



# Inferring the dark matter velocity anisotropy to the cluster edge

Jacob Svensmark<sup>1</sup>,<sup>\*</sup> Steen H. Hansen,<sup>1</sup> Davide Martizzi<sup>1</sup>, Ben Moore<sup>2</sup> and Romaine Tessier<sup>2</sup>

<sup>1</sup>*DARK, Niels Bohr Institute, University of Copenhagen, Jagtvej 128, 2200 København, Denmark*

<sup>2</sup>*Institute for Computational Science, University of Zurich, CH-8057 Zurich, Switzerland*

Accepted 2020 October 5. Received 2020 August 20; in original form 2020 January 6

## ABSTRACT

Dark matter (DM) dominates the properties of large cosmological structures such as galaxy clusters, and the mass profiles of the DM have been inferred for these equilibrated structures for years by using cluster X-ray surface brightnesses and temperatures. A new method has been proposed, which should allow us to infer a dynamical property of the DM, namely the velocity anisotropy. For the gas, a similar velocity anisotropy is zero due to frequent collisions; however, the collisionless nature of DM allows it to be non-trivial. Numerical simulations have for years found non-zero and radially varying DM velocity anisotropies. Here we employ the method proposed by Hansen & Piffaretti, and developed by Høst et al. to infer the DM velocity anisotropy in the bright galaxy cluster Perseus, to near five times the radii previously obtained. We find the DM velocity anisotropy to be consistent with the results of numerical simulations, however, still with large error bars. At half the virial radius, we find the DM velocity anisotropy to be non-zero at  $1.7\sigma$ , lending support to the collisionless nature of DM.

**Key words:** galaxies: clusters: general – dark matter – X-rays: galaxies: clusters.

## 1 INTRODUCTION

The global dynamics of the expanding universe is dominated by two invisible components, namely dark matter (DM) and dark energy (Planck Collaboration et al. 2018). In addition, there exist independent gravitational observations of DM on smaller scales (Clowe et al. 2006). Despite the importance of DM in structure formation, we still have only limited knowledge about its fundamental properties.

From a basic point of view, DM is constituted of fundamental particles, characterized by their mass and interactions with other particles. These parameters can be tested through astronomical observations as well as in terrestrial experiments. Typically, cosmological observations measure a combination of these. For instance, if DM particles interact with photons, structure formation will be affected through the ratio of the interaction cross-section and the DM particle mass,  $\sigma_{\gamma-DM}/M_{DM}$  (Boehm et al. 2002; Hinshaw et al. 2013). Similar constraints can be obtained for DM self-scattering or for various annihilation channels (for a list of references, see e.g. Zavala, Vogelsberger & Walker 2013; Liu, Slatyer & Zavala 2016). A range of accelerator and underground detector ‘null’ observations have provided limits on the DM mass and interaction rates, e.g. from CMS, ATLAS, DarkSide-50, LUX (Faham 2014; Agnes et al. 2015; ATLAS Collaboration et al. 2015; Lowette & CMS Collaboration 2016). Basically, these constraints indicate that the DM has only very limited interactions besides gravity.

Structure formation has been thoroughly investigated for many years using numerical simulations in a cosmological setting. The resulting structures include galaxies and clusters at various stages of equilibration. These simulations have revealed that the DM density profile,  $\rho(r)$ , of individual cosmological structures changes

from having a fairly shallow profile in the central regions,  $\gamma_{\rho} = d \log \rho / d \log r \approx -1$ , to a much steeper fall off in the outer regions,  $\gamma_{\rho} \approx -3$  (Navarro et al. 2010).

For the largest equilibrated structures like galaxy clusters, there is fair agreement between the numerical predictions and observations concerning the central steepness (Pointecouteau et al. 2005; Vikhlinin et al. 2006). However, for smaller structures like galaxies or dwarf galaxies, the observations have indicated that the central region has a shallower density profile than seen in numerical simulations (Gilmore et al. 2007; Salucci et al. 2007), and it is not entirely resolved whether this difference is because of significant self-interaction of the DM, or because of stellar, black hole, or supernova effects. The majority of recent state-of-the-art simulations employing cold DM models with baryonic effects and stellar feedback tend to agree with observations (Teyssier et al. 2013; Amorisco, Zavala & de Boer 2014; Bullock et al. 2015; Wetzel et al. 2016; Santos-Santos et al. 2017; Benítez-Llambay et al. 2018; Dutton et al. 2018; Wheeler et al. 2018); however, some still do not find cores using this approach (Bose et al. 2018). Some efforts have been made with alternative DM models, but the results are thus far not fully conclusive (Di Cintio et al. 2017; González-Samaniego et al. 2017; Fitts et al. 2018).

Observationally, it is very difficult to determine other properties of the DM structures besides the density profile. The density profile is a static quantity (not involving velocity), which arises from the zeroth moment of the Boltzmann equation (i.e. mass conservation). The first moment of the Boltzmann equation instead relates to momentum conservation, and here appears the first dynamical properties in the shape of the so-called DM velocity anisotropy.

The principal purpose of measuring the DM velocity anisotropy is to improve our knowledge of DM. The value of the velocity anisotropy depends on the magnitude of the DM self-interactions (Brinckmann et al. 2018), and hence a precise measurement of the velocity anisotropy in the inner halo region should allow us to

\* E-mail: jacob.svensmark@nbi.ku.dk

constrain the DM collisionality. Furthermore, it has been suggested from theoretical considerations that there should be a correlation between the DM velocity anisotropy and the total mass profile (Hansen 2009), and a future accurate measurement of both would allow testing this prediction. Finally, it is possible that the velocity anisotropy in the outer cluster regions could depend on cosmological parameters, even though, to our knowledge, this has not yet been thoroughly investigated. Hopefully, an investigation like the one we are presenting here will inspire simulators to make such an investigation.

We will in this paper attempt to infer the DM velocity anisotropy of the Perseus galaxy cluster. The technique we use is based only on the observation of hot X-ray-emitting gas, and it uses the combined analysis of both the gas equation (hydrostatic equilibrium) and the Jeans equation with the DM as the dynamical tracer. Measurements and analyses of the X-ray emitting hot gas have improved significantly over the last decades, and we will use the recent observation of Perseus, which extends up to the virial radius (Simionescu et al. 2011; Urban et al. 2014). Here we define the virial radius as the radius where the enclosed density is 200 times the critical density of the universe,  $r_{\text{vir}} = r_{200}$ . This approach of inferring velocity anisotropy contains the radial velocity dispersion of the DM as a degeneracy, and thus the resulting velocity anisotropy should be viewed as a check of the consistency of data with the DM model of the simulation that it inherently relies on.

Probing this dynamical DM property was originally suggested in Hansen & Piffaretti (2007); however, the first reliable estimate was made by stacking 16 galaxy clusters (Host et al. 2009). This stacked cluster inference extended to approximately 0.85 times  $r_{2500}$ . Thus, in this paper, we will extend this inference by approximately a factor of 5 in radius. The following sections outline how this is done through our implementation of this method in the context of the Perseus observations.

## 2 HYDROSTATIC GAS AND EQUILIBRATED DM

The conservation of momentum for a fluid leads to the Euler equations, which, for spherical and equilibrated systems, reduce to the equation of hydrostatic equilibrium,

$$\frac{GM(r)}{r} = -\frac{k_b T_{\text{gas}}}{m_p \mu_{\text{gas}}} \left( \frac{\partial \ln \rho_{\text{gas}}}{\partial \ln r} + \frac{\partial \ln T_{\text{gas}}}{\partial \ln r} \right). \quad (1)$$

This equation simply states that when we can measure the gas temperature and gas density (all quantities on the right-hand side of this equation) then we can derive the total mass profile. From the total mass profile, one can then derive the DM density profile. The gas properties are typically observed through the X-ray emission from bremsstrahlung, and this X-ray determination of the DM density profile is very well established (Sarazin 1986). Alternatively, both density and temperature profiles can in principle be measured separately through the Sunyaev–Zeldovich effect.

Let us now consider the dynamical equation for the DM. The DM is normally assumed to be collisionless, and hence the fluid equations do not apply. Instead, one starts from the collisionless Boltzmann equation. The first moment of the collisionless Boltzmann equation leads to the first Jeans equation, which for spherical and fully equilibrated systems reads (Binney & Tremaine 2008)

$$\frac{GM(r)}{r} = -\sigma_r^2 \left( \frac{\partial \ln \rho}{\partial \ln r} + \frac{\partial \ln \sigma_r^2}{\partial \ln r} + 2\beta \right). \quad (2)$$

If we look at the right-hand side of the Jeans equation, we see that there are three quantities: the DM density,  $\rho(r)$ , the radial velocity dispersion, and the velocity anisotropy,

$$\beta \equiv 1 - \frac{\sigma_\theta^2 + \sigma_\phi^2}{2\sigma_r^2}, \quad (3)$$

where  $\sigma_r^2$ ,  $\sigma_\theta^2$ , and  $\sigma_\phi^2$  are the velocity dispersions of DM along the radial, polar, and azimuthal directions, respectively.

We can infer the total mass and the DM density from the equation of hydrostatic equilibrium. That means that if we wish to determine the velocity anisotropy, then we must find a way to obtain the radial velocity dispersion of the DM,  $\sigma_r^2$ . To that end, we will need assistance from numerical simulation, which we will explain in detail below. The conclusion will be that we can map the gas temperature to the DM velocity dispersion. Thus, the inference of the DM velocity anisotropy depends on the ability of numerical simulations to reliably map between gas temperature and DM dispersion.

The DM particles are normally assumed to be collisionless, and hence the haloes of DM will never achieve a thermal equilibrium with Maxwellian velocity distributions (Chapter 4 in Hansen et al. 2006; Binney & Tremaine 2008). Therefore, the DM cannot formally be claimed to have a ‘temperature’. However, for normal collisional particles, there is a simple connection between the thermal energy of the gas and the temperature, and we use a similar terminology for DM, and hence discuss its ‘temperature’ as a representation of its local kinetic energy:

$$T_{\text{DM}} \equiv \frac{m_p \mu_{\text{DM}}}{3k_b} \sigma_{\text{DM}}^2, \quad (4)$$

where the total dispersion is the sum of the three one-dimensional dispersions:

$$\sigma_{\text{DM}}^2 \equiv \sigma_r^2 + \sigma_\theta^2 + \sigma_\phi^2. \quad (5)$$

Since the DM and gas particles inside an equilibrated cosmological structure experience the same gravitational potential, we should expect the gas and DM temperatures to be approximately equal (Hansen & Piffaretti 2007). Later analyses have shown (Host et al. 2009; Hansen et al. 2011) that the ratio of DM to gas temperatures,

$$\kappa \equiv \frac{T_{\text{DM}}/\mu_{\text{DM}}}{T_{\text{gas}}/\mu_{\text{gas}}}, \quad (6)$$

is a slowly varying function of radius, always of the order unity.

## 3 DM VELOCITY ANISOTROPY FROM OBSERVABLES

The Jeans equation can be rewritten as

$$\beta = -\frac{1}{2} \left( \frac{\partial \ln \rho}{\partial \ln r} + \frac{\partial \ln \sigma_r^2}{\partial \ln r} + \frac{GM(r)}{r \sigma_r^2} \right). \quad (7)$$

We will now clarify how the three terms on the right-hand side can be expressed as functions only of the measured gas temperature and density, and also the calibration of  $\kappa$  from numerical simulations. As discussed above, by measuring the gas temperature and density, the equation of hydrostatic equilibrium, equation (1), gives us the total mass profile. In addition, this allows us to derive the DM density profile,  $\rho = \rho_{\text{tot}} - \rho_{\text{gas}}$ . Thus, we only need an expression for the radial velocity dispersion of the DM,  $\sigma_r^2$ . Combining the definitions in equations (3)–(6) gives

$$2\sigma_r^2 \beta = 3\sigma_r^2 - 3 \frac{k_b T_{\text{gas}}}{m_p \mu_{\text{gas}}} \kappa. \quad (8)$$

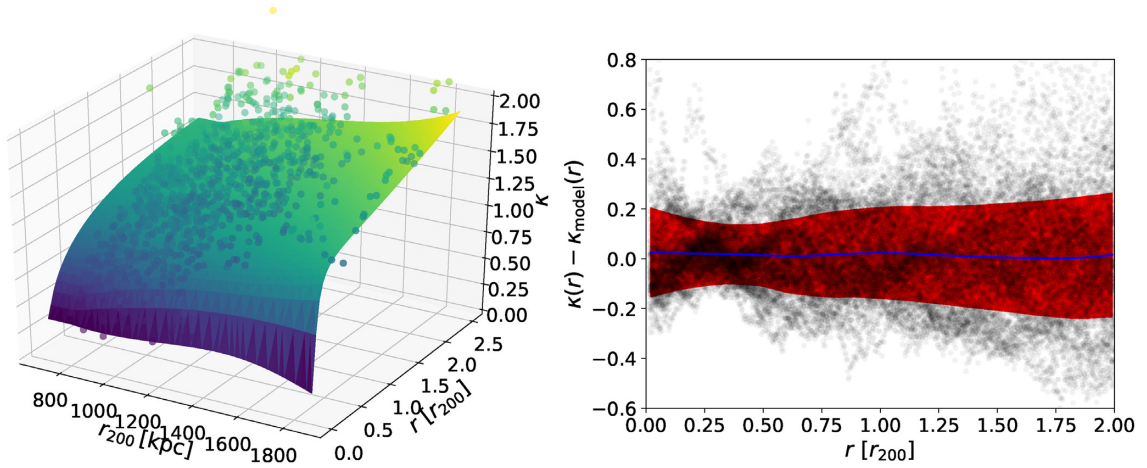


**Figure 1.**  $\kappa$  profiles for the 51 clusters of the RAMSES simulation, as function of radius and  $r_{200}$ . The left-hand panel shows a 2D smoothing spline to the profiles, and the right-hand panel shows the  $1\sigma$  scatter contours of the residuals collapsed along the  $r_{200}$  direction. The smoothed surface, and scatter profile serves as parametrization for  $\kappa(r, r_{200})$  profiles for observations.

This allows us to rewrite the Jeans equation as

$$\sigma_r^2 \left( \frac{d \ln \rho_{\text{DM}}}{d \ln r} + \frac{d \ln \sigma_r^2}{d \ln r} + 3 \right) = \psi(r). \quad (9)$$

where the quantity

$$\psi(r) = \left( \frac{3k_b}{m_p} \frac{T_{\text{gas}}}{\mu_{\text{gas}}} \kappa - \frac{GM(r)}{r} \right) \quad (10)$$

contains quantities from the X-ray observables, as well as  $\kappa$ . Equation (9) can be solved as

$$\sigma_r^2(r) = \frac{1}{\rho_{\text{DM}} r^3} \int_0^r dr' \psi(r') \rho_{\text{DM}}(r') r'^2, \quad (11)$$

through numerical integration. The solution to the integral depends on the boundary condition on  $\sigma_r$ . Here we assume that  $\sigma_r^2(0) = 0$ . In this way, we have all the quantities on the right-hand side of equation (7), and  $\beta$  can directly be calculated.

#### 4 NUMERICAL SIMULATION AND PARAMETRIZING $\kappa$

The energy argument that the DM dispersion should be approximately equal to the gas temperature ( $\kappa \approx 1$ ) in relaxed gravitating structures has a long history (Sarazin 1986). The anticipation that  $\kappa$  may change significantly when gas is cooling was investigated by Hansen et al. (2011), where  $\kappa$  was extracted for Milky Way like galaxies as a function of redshift (where cooling is extremely much more significant than in cluster outskirts). There it was found that as long as the high-density/low-temperature component of the gas is removed,  $\kappa$  remains close to unity around  $z = 0$ .

Here we take possibly the most modern approach to gas cooling and other radiative processes in simulation to extract  $\kappa$ . We chose to use a simulation with the AMR code RAMSES (Teyssier et al. 2002), which uses flat Lambda cold dark matter ( $\Lambda$ CDM) cosmology with cosmological constant density parameter  $\Omega_\Lambda = 0.728$ , matter density parameter  $\Omega_m = 0.272$  of which the baryonic density parameter is  $\Omega_b = 0.045$ , power spectrum normalization  $\sigma_8 = 0.809$ , primordial power spectrum index  $n_s = 0.963$ , and current epoch Hubble parameter  $H_0 = 70.4 \text{ km s}^{-1} \text{ Mpc}^{-1}$ . To identify large galaxy clusters, the simulation was initially run as a DM-only simulation with comoving box size  $144 \text{ Mpc } h^{-1}$  and particle mass

$m_{\text{DM}} = 1.55 \times 10^9 \text{ M}_\odot h^{-1}$ . Here  $h$  is the dimensionless Hubble parameter, defined as  $h = H_0/100 \text{ km s}^{-1} \text{ Mpc}^{-1}$ . After running the DM-only simulation, 51 cluster-sized haloes with total masses above  $10^{14} \text{ M}_\odot h^{-1}$  were identified and re-simulated including the baryonic component, with DM particle mass  $m_{\text{DM}} = 1.62 \times 10^8 \text{ M}_\odot h^{-1}$  and baryonic component mass resolution of  $3.22 \times 10^7 \text{ M}_\odot$ . The 51 re-simulation runs implemented models of radiation, gas cooling, star formation, metal enrichment, supernova, and AGN feedback, and were evolved to  $z = 0$ . A detailed description of the simulation can be found in Martizzi et al. (2014).

For the 51 clusters, the  $\kappa$  profile can be calculated in spherical bins according to equation (6). Since all quantities contained in  $\kappa$  depend on the cluster size, we calculate a 2D smoothing spline surface for the 51  $\kappa(r, r_{200})$  profiles, such that given  $r_{200}$  for a cluster,  $\kappa(r)$  can be retrieved (left-hand panel of Fig. 1). The error associated with using this  $\kappa$  function is approximated from the residual after collapsing it in the  $r_{200}$  direction (Fig. 1, right-hand panel), and we find no strong correlation or systematics within these residuals. The resulting  $1\sigma$  standard deviation profile can then be taken into account when inferring  $\beta(r)$ .

In Fig. 2, we show how previous  $\kappa$ -estimates compare to the one(s) we use here. Profiles from the fitted smoothing spline surface are shown for three cluster sizes: 700, 1200, and 1700 kpc. We find  $\kappa$  to increase with cluster size on the displayed radial range. Sarazin (1986) assumed  $\kappa = 1$ , which is obviously a first approximation, but depending on the cluster size, reasonable within  $0.3r_{200}$ . Later numerical approaches, such as the use of gadget-2 (Kay et al. 2007) (previously used to extract  $\kappa$ ; Host et al. 2009), yield a similar  $\kappa$ . Host et al. (2009) include radial constraints and an error band around  $\kappa = 1 \pm 0.1$ , shown as the black shaded area on Fig. 2. The size range of the clusters considered in Host et al. (2009) is comparable to the green curve in Fig. 2, and they are found to be consistent within error bars. In Fig. 2, the lower  $\kappa$  limit of Host et al. (2009) is truncated at  $0.1r_{200}$ . At lower radii, the effects from AGN feedback become relevant, which was not included in the gadget-2 simulations. A first step towards including AGN feedback was done in fig. 7 of Hansen et al. (2011). Here a clear AGN effect is seen in the inner parts of the cluster in their conservative AGN feedback model estimate. Note that for this figure, we have taken into account that they use a different definition of the calibration between gas and DM temperatures. As gas temperature increases towards



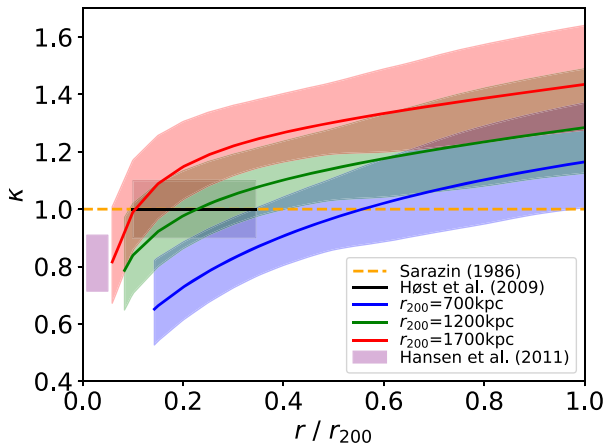


**Figure 2.** Comparison of  $\kappa$  profiles used here and in previous works (Sarazin 1986; Host et al. 2009). Bands on the curves display  $1\sigma$  spread of the  $\kappa$  profiles. Note that in Sarazin (1986),  $\kappa = 1$  by assumption, so no error bands are shown here. The purple band of Hansen et al. (2011) shows the approximate area in which their curve varies.

the cluster centre,  $\kappa$  (in our definition) decreases, which results in a sharp decrease. This decrease, shown as an approximate purple square in Fig. 2, is consistent with the decrease we observe in our  $\kappa$  profiles, which are based on simulations that take a more advanced approach to implementing AGN feedback. One could imagine further explorations of  $\kappa$ . We have performed some preliminary investigation on  $\kappa$  parametrization based on relaxedness, and found that while it adds to  $\kappa$  scatter, the effect was subdominant to the cluster size effect. Relaxedness, presence of a cool core, triaxiality, and other effects could however be subjects for future study.

Herein lies the core of the method, but notably also the reason why resulting  $\beta$  profiles cannot be called *de facto* measurements. Rather they are consistency checks with the DM model employed in the simulation that produces the  $\kappa$  relation. The Jeans equation assumes DM to be collisionless, as (in this case) does the simulation that produces  $\kappa$ ; however, should this assumption not be valid, a measured  $\beta$  profile might not be consistent with those of simulations. From an observational point of view, the  $\kappa$ -parametrization makes good sense, as measurements of the mass profile and thus  $r_{200}$  of galaxy clusters are independent of  $\kappa$ . Thus, by observing the properties of the hot X-ray-emitting gas, we can obtain  $\kappa(r)$  using our parametrization, and from this calculate  $\sigma_r^2(r)$  from equation (9) and, finally,  $\beta(r)$  from equations (6) and (8), assuming that the gas is fully equilibrated. The next section is dedicated to reinforcing the soundness of this assumption in the observations that we choose to analyse.

## 5 EXCLUDING INFEASIBLE SECTORS FROM ANALYSIS

One of the core assumptions in deriving mass profiles from the X-ray signal in galaxy clusters is that of hydrostatically equilibrated gas. This excludes a large block of potential cluster targets for study, as merging and other irregularities causes a failure to meet this demand. Previous studies show how cluster merging can cause cold front and sloshing in the hot baryonic gas, and phenomena that show up in derived X-ray profiles as unequilibrated features (Markevitch & Vikhlinin 2007). Data quality has however heightened through the last decades, and so has the frequency of attempts at solving this issue through data selection – considering only sections of the

observational plane that best meets the assumptions of equilibrium. This makes sense if material falling on to an equilibrated structure is small enough to only disturb equilibrium locally, or that the infalling material has not yet had time to perturb the larger equilibrated cluster in its entirety.

In order to develop and test a method of inferring  $\beta$  to high radii through data selection in the observational plane of galaxy clusters, we construct a mock observational catalogue from the RAMSES re-simulated clusters. Radial profiles of all quantities relevant for the present work has been extracted. We select a subsample of 10 randomly selected clusters in range  $14 < \log m_{200} < 15$ , where half of the clusters in the sample have been classified as globally relaxed, following the criterion of Martizzi & Agrusa (2016). We choose a line of sight through them at random and divided each observational plane of the 10 clusters into eight equiangular sectors. The motivation for this division originates in the Perseus X-ray observations analysed in the next sections. Perseus is precisely observed along eight arms at evenly spaced angles, yielding eight gas density and temperature profiles in total for the cluster. Previous analysis of the eight arms of Perseus has shown signatures of cold fronts and sloshing of the gas in five of the eight arms, suggesting that they are suboptimal for calculations assuming hydrostatic equilibrium. The remaining three are shown to be more relaxed. In the following, we take a similar approach selecting just the sectors that are equilibrated. We conclude that by deselecting the most deviant sectors, we can reduce the scatter in our final inference of  $\beta$  within the RAMSES clusters.

For each of the sectors in the observational plane, 3D radial profiles from spherical shells were extracted for the gas and DM component, using only the particles that, in projection, are contained inside of that sector. Each sector can then be analysed separately, and thus parts of the observed cluster that displays unequilibrated features may be excluded from our calculation of  $\beta(r)$ . With this in hand, we estimate the statistical reward in removing sectors from analysis, and use this in an attempt to reduce the error bars of  $\beta(r)$  for actual X-ray data.

Fig. 3 displays gas temperature and density profiles for 6 of the 10 re-simulated galaxy clusters for which we have 3D data. The remaining four clusters displayed enough unequilibrated features in the gas component that they were unfit to consider for further analysis, due to strongly inconsistent profiles across the eight sectors of a cluster, or a steep incline in the central temperature profiles. It should be noted that only three of the six clusters remaining were categorized as virialized using the criteria of Martizzi & Agrusa (2016). Each column of Fig. 3 represents one of the six clusters, and the coloured profiles represent individual sectors. Top panels show the gas temperature scaled by a constant, and the central panels show the gas density also scaled. From these two quantities alone, it is clear that sectors within a single cluster display some variance, which is natural to expect from a 3D numerical simulation, but also a reflection of the hydrostatic equilibrium assumption not being perfectly true. For the remainder of this section, we will discuss which directions appear less equilibrated than others, considering purely the observational gas profiles.

For some of the clusters, looking only at the top two rows of Fig. 3, it is not always easy to tell whether parts of the cluster are effected by some disturbing element. The fifth column has a pretty clear signature in the temperature profiles that something is disturbing its equilibrium in the dark blue, purple, and pink sectors. For the cluster in the sixth column, deviations from hydrostatic equilibrium are more subtle. Herein lies an observational challenge, and in an attempt to enhance the visibility of such subtle differences between sectors within a single galaxy cluster, we combine the two measurable quantities  $\rho_{\text{gas}}$  and  $T_{\text{gas}}$  into a single quantity.

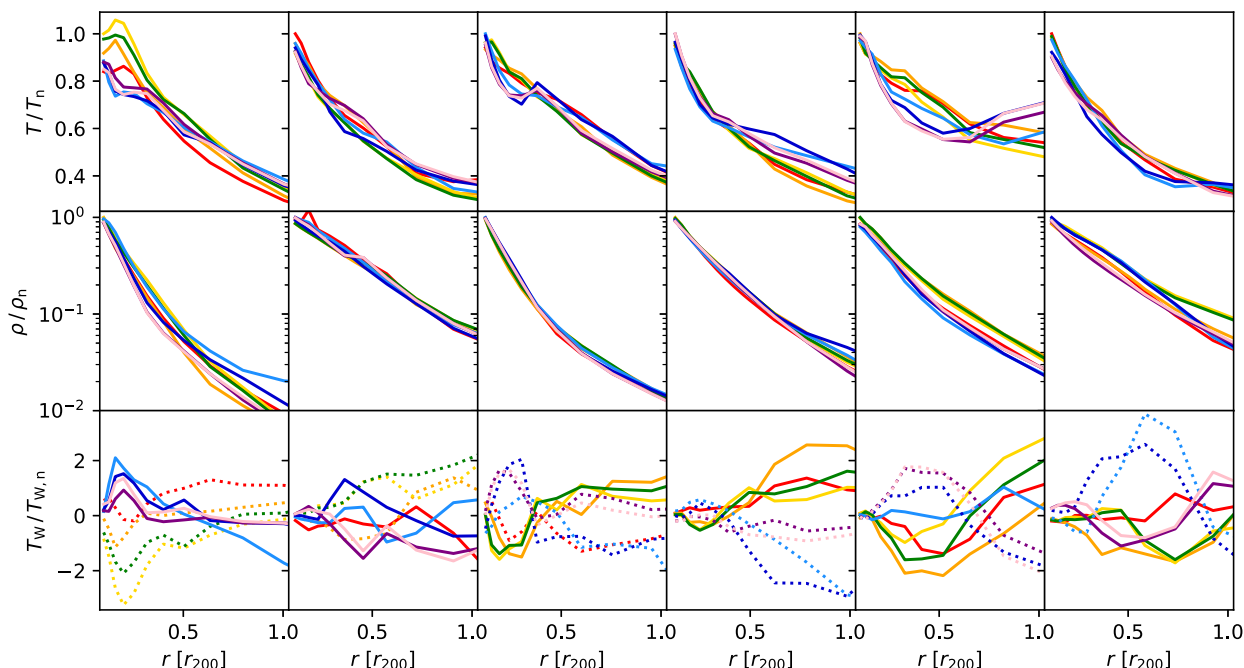


**Figure 3.** Temperature profiles (top row), gas density profiles (middle row), and weighted temperature variation profiles (bottom row) for the six re-simulated RAMSES clusters considered for analysis. Each colour represents one of the eight sectors within the cluster. Neighbouring sectors are coloured in the following order: red, orange, yellow, green, light blue, dark blue, purple, and pink. The dotted profiles in the bottom row indicates the sectors that were excluded from analysis due to their profile as discussed in the main text. Note that  $T$ ,  $\rho$ , and  $T_w$  profiles are scaled by a constant  $T_n$ ,  $\rho_n$ , and  $T_{w,n}$ , which differs within each cluster, in order to compare profile shapes between clusters in this figure.

The bottom panels of Fig. 3 show this combination in the form of a weighted temperature variation profile,

$$T_w = \rho_{\text{gas}} r^2 \left( 1 - \frac{T_{\text{gas}}}{\overline{T_{\text{gas}}}} \right), \quad (12)$$

where  $\overline{T_{\text{gas}}}$  is the mean temperature profile of the entire cluster. This observationally available construct emphasizes in some cases distinct groups of sectors, and by comparing these to the gas and temperature profiles of the same cluster, we try to deselect those that are least consistent with the overall trend of the cluster. Here bumps, i.e. cold fronts in the temperature and density profile, are features we look for (Markevitch & Vikhlinin 2007). In the case of well-behaved clusters, this of course is less obvious, and arguably data selection may also have less of an effect. In column 3 of Fig. 3, the density is smooth, but the dark blue, light blue, pink, purple, and red directions have a bump in the temperature profile. The  $T_w$  profiles show two groups that clearly differ from each other. Based on the irregular bump in the  $T_{\text{gas}}$  profile and the separation in the  $T_w$  figure, we include only the green, orange, and yellow directions, and indicate the deselected sectors with the grey colour in the bottom panel. In column 6, the two blue sectors stand out slightly in the  $T_{\text{gas}}$  profile, but more profoundly in the  $T_w$  profile, and are thus removed from analysis. Column 2 displays a very smooth cluster, and it is less clear which (if any) directions should be removed. We deselect the green, yellow, and orange directions as they tend to lie slightly high for the high radii of primary interest for this paper. The cluster in the first column shows a kink towards its inner parts. Here, the red, orange, green, and yellow profiles deviate largely within  $0.7r_{200}$  from the remaining four sectors, and are thus removed from analysis. The  $T_w$  profiles of column 4 shows three main groups, substantiating what is otherwise hard to see in the  $T_{\text{gas}}$  profiles alone. We remove from

analysis the dark blue, light blue, purple, and pink, and keep the most coherent four sectors as indicated in the figure.

In some clusters, such as the one in column 5 of Fig. 3, signatures of a ‘cold-front’ are visible in the sectors represented by the dark blue, pink, and purple profiles, which are consequently removed from analysis. These may be caught by performing an analysis of the X-ray data analogous with the one in Urban et al. (2014), and, in this case, both approaches would possibly single out the same sectors. The present exclusion process however singles out some features that are not predominantly cold-front-related, and as such provides a different approach to determining which parts of a galaxy cluster that are not in equilibrium.

From the weighted temperature variation profiles in combination with the raw density and temperature profile, we have identified up to five sectors within each cluster that deviate substantially from the more relaxed conditions, and are now ready to calculate the velocity anisotropy parameter  $\beta$ .

## 6 NON-PARAMETRIC FITTING AND MC RESAMPLING TO DATA

In order to arrive at an inference of  $\beta$ , local fluctuations and measurement uncertainties are necessary to take into account. We employ non-parametric locally estimated scatter plot smoothing (LOESS) fitting to the gas density and temperature measurements in order to smooth out local variations (Scrugga 2011). In this way, we manage to avoid imposing an analytical profile to our data. This yields a fitted curve and a  $1\sigma$  standard deviation profile in addition. Any fit, including this one, is of course subject to a level of arbitrariness in the choice of function, and for non-parametric fits, some choice of smoothing parameter and algorithm. In this case, we

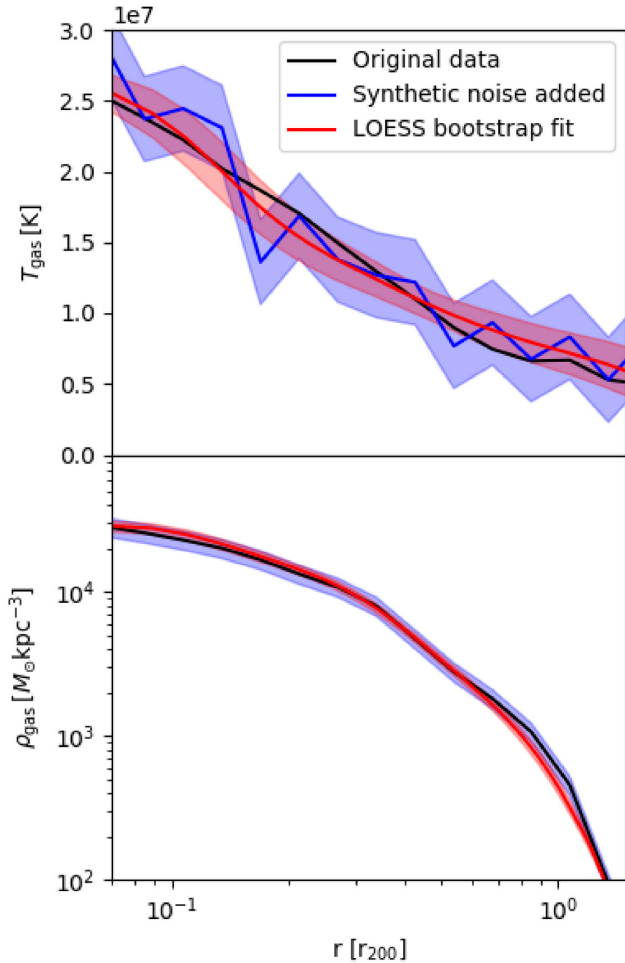


**Figure 4.** Example of the temperature (upper panel) and density (lower panel) LOESS fits employed in the hydrostatic equilibrium calculation for the gas component, as applied to a single clean sector from one of the RAMSES-simulated clusters. The top panel shows  $T_{\text{gas}}$  and the bottom panel  $\rho_{\text{gas}}$ . Black lines show the original profiles. The blue curves and patches shows the profile with synthetic noise and error bars added, and the red curves shows the median and 68 per cent percentile of 100 bootstrap resampled Monte Carlo LOESS fits to the noisy profiles.

let the LOESS smoothing parameter be determined by a generalized cross-validation technique (Wang 2010), which adapts to the data in question. Doing this, we obtain a smooth profile that neglects local bumps and wiggles, however allowing for larger scale variation, rather than forcing it to follow a strict parametric form. An example of a cross-validated LOESS fit to the gas temperature profile is seen in Fig. 4 for a single sector in one of the galaxy clusters within the RAMSES simulation. In this example, the temperature profile from the simulated data is without uncertainty and smooth in comparison with realistic measurements of the 3D temperature profiles of galaxy clusters. Therefore, Gaussian errors of  $3 \times 10^6$  K and error bars of the same magnitude are added. The red band of Fig. 4 represents the 68 per cent percentile of 100 LOESS fit to the noisy data using a resampling technique assuming a Gaussian distribution, and recreates the original temperature profile in black reasonably well. The same goes for the  $\rho_{\text{gas}}$  in the bottom panel, though this is to be expected as uncertainties in typical gas density profiles are small compared to the temperature measurements. As explained in Section 7, we employ a Monte Carlo resampling approach to obtain error estimates on

the inferred galaxy cluster  $\beta$ . For an input smoothed  $T_{\text{gas}}$  and  $\rho_{\text{gas}}$ , we proceed to calculate  $M(r)$ ,  $\sigma_r^2(r)$  and  $\beta(r)$  through hydrostatic equilibrium assumptions, as shown in Section 2. In this process, we fit yet another LOESS curve to both the  $M(r)$ ,  $\rho$  and  $\sigma_r^2(r)$  profiles, to neglect the smaller bumps and ripples. This comprises the drawback of not assuming and fitting e.g. well-behaved power-law functions to the raw hydrostatic data. However, the multiple non-parametric fits do allow a degree (as controlled by the cross-validation mentioned above) of ripple that would otherwise not be seen in the parametric form, and, in this respect, the approach is arguably preferable. In the next section, we can begin the process of Monte Carlo resampling  $\rho_{\text{gas}}$ ,  $T_{\text{gas}}$ , and  $\kappa$  to arrive at a final inference of  $\beta$  and its uncertainty from a number of sectors within a single galaxy cluster.

## 7 ERRORS IN ESTIMATING $\beta$

Each sector of each cluster is handled individually in our analysis. The final  $\beta$  of a given sector is obtained using a Monte Carlo resampling approach, which allows us to propagate measurement errors from the input X-ray profiles. For a single sector, we produce a number  $N_{\text{MC}}$  of resamples of  $T_{\text{gas}}(r)$  using its measurement uncertainties. We resample complementary  $\kappa(r)$  profiles and proceed to calculate  $M(r)$ ,  $\sigma_r^2(r)$  and  $\beta(r)$  through hydrostatic equilibrium assumptions, as shown in Section 2 and 6. The final  $\beta$  profile for a given sector is then the median profile of all  $\beta$  from the resamples of that sector.

Our intent is to use the procedure on multiple sectors of a single cluster (or potentially even multiple clusters, though this is left for future work), and end up with a final inference of the universal velocity anisotropy profile. We must therefore understand to what degree the procedure is biased, and how much scatter it introduces in addition to the natural scatter within cluster  $\beta$  profiles. To do this, we infer the  $\beta$  profile of two groups of sectors from the six RAMSES clusters selected in Section 5: one group consisting of all 48 sectors in the six RAMSES clusters, and another group using only the 27 equilibrated sectors. Starting with the full set, as an intermediary step the hydrostatic mass profiles of each sector is calculated. These can be seen in Fig. 5, relative to the true mass profiles. The hydrostatic masses are just within the  $1\sigma$  standard deviation profile at the radii of interest, however the mean value underperforms between between 0 and 10 per cent low for growing radii similar to previous findings using other mass reconstruction techniques (Gifford & Miller 2013; Armitage et al. 2018). One could imagine correcting inferred masses accordingly; however, it is non-trivial how that translates into a  $\beta$  correction given the simulated data we have available. For this reason, we allow the hydrostatic mass measurements to underperform at these radii.

Proceeding towards  $\beta$ , Fig. 6 on the left shows in the red curve and red band a LOESS fit and  $\sigma$  scatter of the true  $\beta$  profiles for the full set of sectors. The black curve and grey band show the same, but for the  $\beta$  profiles as inferred from only the gas observables of each sector. The mock inference of  $\beta$  in a sector is seen to be unbiased, with a scatter determined largely by the true scatter in  $\beta$  until around  $0.5 r_{200}$ , at which point the scatter is dominated by assumptions of equilibrium breaking down. In order to lessen the scatter, only the sectors selected in Section 5, i.e. the second set of sectors, were used, and their true and inferred  $\beta$  summarized in the right-hand side of Fig. 6. Notably, the scatter is lower in this case because assumptions of equilibrium are better met in these selected simulated sectors.

The grey patches in the right-hand panel of Fig. 6 comprises scatter in the true  $\beta$  profiles of the simulated clusters, as well as additional scatter introduced by our analysis. As we proceed to calculate  $\beta$  for X-ray observations of the sectors in a single real galaxy cluster, we

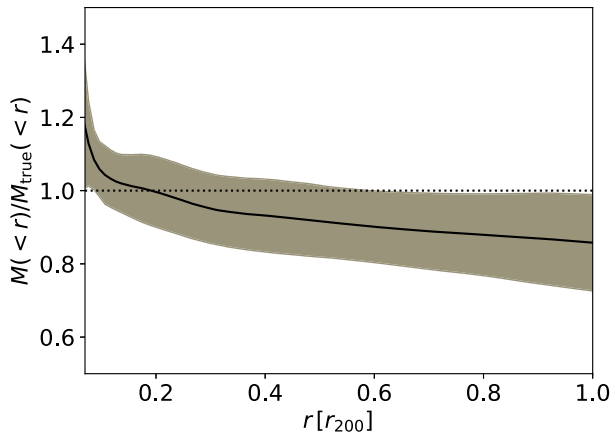


**Figure 5.** The mass profiles from hydrostatic equilibrium for all sectors of the six RAMSES clusters relative to the true mass profile of the cluster they belong to. The black curve represents a LOESS fit to the individual profiles, and the grey band represents the  $1\sigma$  standard deviation of the profiles, as obtained from the generalized cross-validation technique of the LOESS fit outlined in the main text.

must incorporate this scatter in the uncertainty of our inference. How this is done depends on the amount of correlation between sectors of a single galaxy cluster. If all sectors within a single cluster are completely independent inferences of  $\beta$ , then the uncertainty of the joint  $\beta$  profile decreases by a factor  $1/\sqrt{N}$ , where  $N$  is the number of sectors under analysis. If, on the other hand, sectors within a single cluster are completely correlated, the part of the scatter that originates from natural variation in  $\beta$  (red patch of Fig. 6) is constant with number of sectors, whereas the residual scatter (difference between grey and red scatter) in Fig. 6, i.e. the additional scatter introduced by the analysis framework, is reduced by  $1/\sqrt{N}$ , assuming that the two sources of scatter are directly separable. As one extreme we could assume that all of the sectors of a single galaxy were uncorrelated in their inference of  $\beta$ , and as another we could assume complete correlation.

Now we have an estimate of the uncertainties involved in inferring  $\beta(r)$  through X-ray data and assumptions of hydrostatic equilibrium, and a method for eliminating parts of this uncertainty by data

selection. In the next section, we move to apply the technique and infer  $\beta(r)$  to the virial radius for the Perseus galaxy cluster.

## 8 PERSEUS CLUSTER OBSERVATIONS IN X-RAY

The Perseus cluster is the brightest cluster in the X-ray sky, and was observed in 85 pointings as a Suzaku Key Project, with a total exposure time of 1.1 Ms. The low particle background makes Suzaku ideal for analysing cluster outskirts. These pointings were arranged in eight arms along different azimuthal directions. For each direction, the data had point sources removed and were cleaned, 21 pointings were used for a careful background modelling, and XSPEC was used to extract the deprojected temperature and density profiles (Simionescu et al. 2011; Urban et al. 2014). Such careful treatment of the deprojection is necessary, as the calculation of  $\beta$  requires 3D profiles of  $T_{\text{gas}}$  and  $\rho_{\text{gas}}$  to function. For each of the eight arms, the  $T_{\text{gas}}$  and  $\rho_{\text{gas}}$  profiles can be seen with uncertainties in the top and middle panels of the left-hand side column in Fig. 7.

Previous careful analyses allowed a categorization of the eight arms into three ‘relaxed’ arms showing no particular irregular behaviour, where, in particular, the temperature profiles are generally decreasing functions of radius. The other arms either show signs of large cold fronts between 20 and 50 arcmin from the centre, or showed signs of large-scale sloshing motion of the gas (Simionescu et al. 2011, 2012; Urban et al. 2014).

In this work, we consider temperature variations relative to the mean profile, and weigh them by  $\rho r^2$  as described in equation (12). The  $T_{\text{W}}$  profiles are seen in the bottom panel of the first column in Fig. 7. Since Perseus is already a comparatively virialized cluster, there are not a couple of sectors that show extremely obvious deviant features from the mean temperature profile. The western arm (magenta) shares more or less no features with the rest, and is arguably not in equilibrium with the remaining parts of the cluster. Beyond  $0.7 r_{200}$ , the spread of the profiles becomes very large and the profiles deviate significantly from each other. Within  $0.7 r_{200}$ , the eastern (black), north-eastern (red), and, to a lesser extent, the south-eastern (brown) arms display an irregularity that Urban et al. conclude to be a cold front. Here we shall remove eastern and north-eastern arms, the ones furthest from the mean temperature profile below

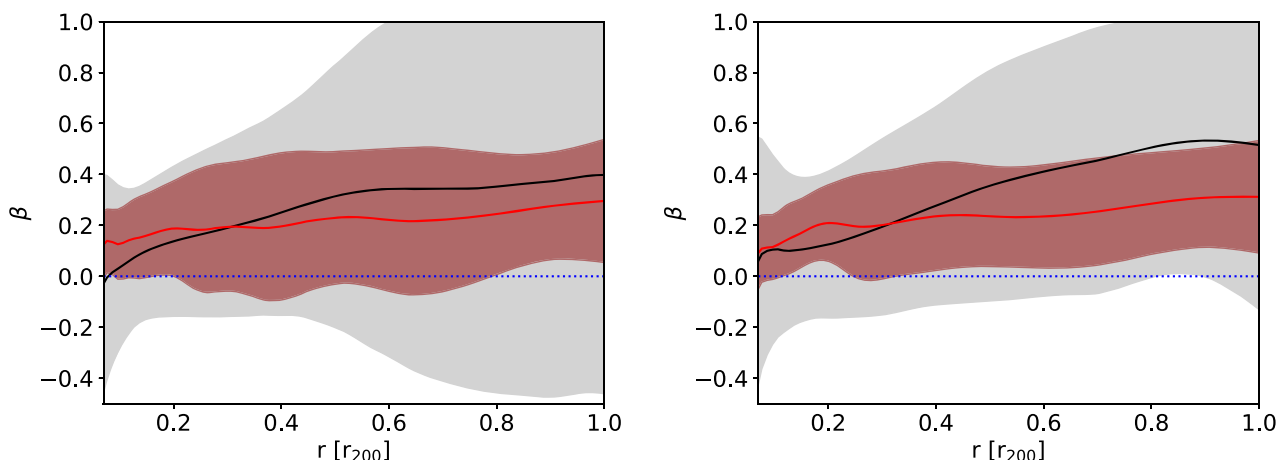


**Figure 6.**  $\beta$  profile for all sectors (left-hand panel) and selected sectors (right-hand panel) for the six relaxed RAMSES clusters using interpolated 2D smoothing spline  $\kappa$  profiles for each cluster. The red curve shows a LOESS fit to the true  $\beta$  profiles, and black curves to inferred ones. The red narrow patches indicate the  $1\sigma$  standard deviation of the true  $\beta$  profiles, and the light grey wider patches indicated the same but for the inferred  $\beta$  profiles, as obtained through the generalized cross-validation technique of the LOESS fit outlined in the main text. Thus, the standard deviations shown here is for a single sector of a single cluster.



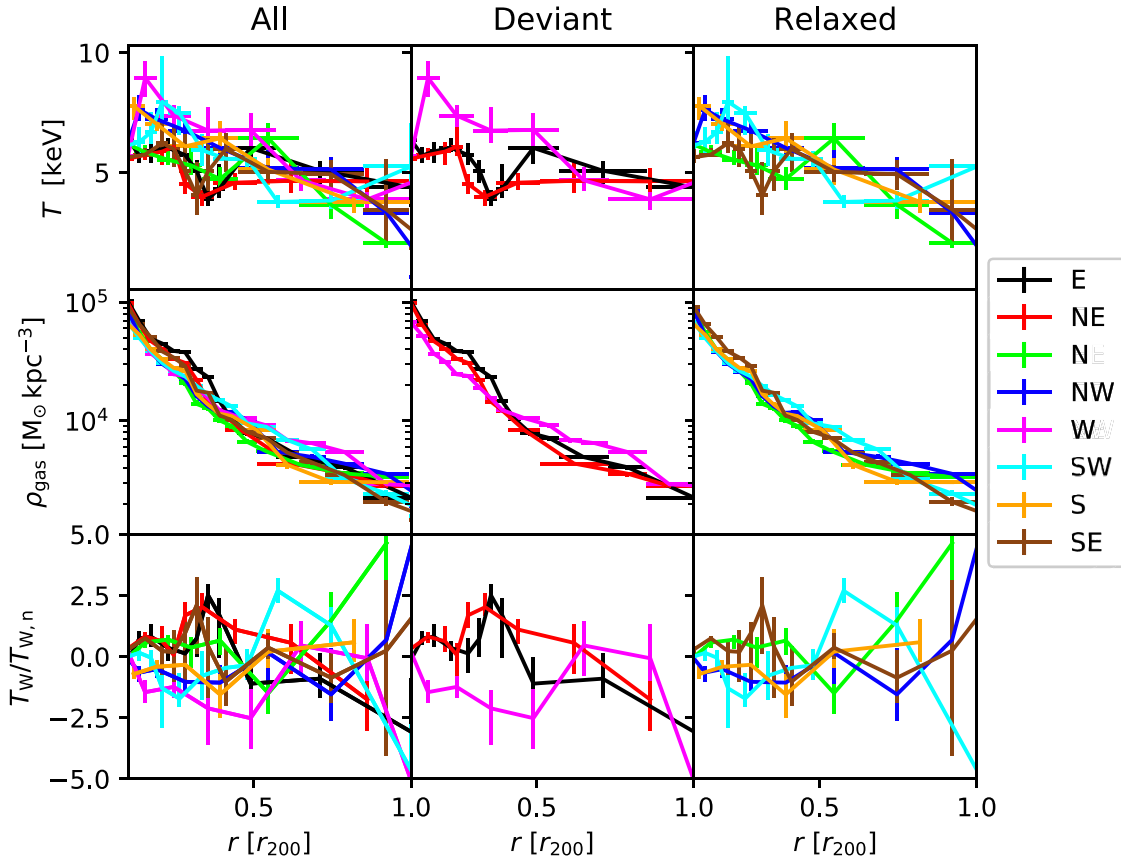


**Figure 7.** Deprojected profiles for the eight sectors of the Perseus cluster, grouped in categories through columns ‘All’, ‘Deviant’, and ‘Relaxed’. The top row shows the gas temperature  $T_{\text{gas}}$ , middle row the gas density  $\rho_{\text{gas}}$ , and bottom row the weighted temperature variation  $T_{\text{W}}$ .

$0.5r_{200}$  and with a general downwards tendency beyond  $r_{200}$  in the  $T_{\text{W}}$  profiles (Fig. 7, bottom row, central column). Instead, we focus on the remaining five profiles closer to the mean below  $r_{200}$  and with the upwards tendency in the  $T_{\text{W}}$  profiles beyond  $r_{200}$  (Fig. 7, bottom row, third column). Then we are consistent with the methodology of the previous sections, where the numerical clusters were considered, and arrive at the selections in the third column of Fig. 7. The middle column shows the profiles that are not included in the analysis.

This leaves us with three sets of data within Perseus: the full set, the sectors selected here, and the ones found to be relaxed by previous analysis (Urban et al. 2014). In the following section we examine all three sets. Each arm is fed through our analysis separately, and in the end we stack the  $\beta$  of each set to obtain an overall inference of  $\beta$  from Perseus.

We do not consider radii outside the virial radius, where the infall motion leads to departure from hydrostatic equilibrium (Falco et al. 2013; Albæk et al. 2017).

## 9 EXTRACTING THE DM VELOCITY ANISOTROPY IN PERSEUS

Having prepared a method for data selection in the previous sections, and determined three sets of sectors for the Perseus cluster to investigate, we are now ready to extract  $\beta$  from it. We use the deprojected observations of  $T_{\text{gas}}$  and  $\rho_{\text{gas}}$  profiles and their corresponding error bars to perform a Monte Carlo sampling as input for the analysis for each sector, i.e. each arm. First,  $\partial \ln \rho_{\text{gas}} / \partial \ln r$  and  $\partial \ln T_{\text{gas}} / \partial \ln r$  are

found at each radial point by computing central differences in the interior and first differences at the boundaries. These are then used in the hydrostatic equilibrium equation to calculate the mass profile. This mass profile is again subjected to a non-parametric LOESS fit in order to smooth out bumps and wiggles. After subtracting the gas mass, we can directly generate the DM density profile. The resulting mass profile of Perseus can be seen in Fig. 8, using the data from all eight arms. For each Monte Carlo sampling, a DM temperature profile is also resampled based on the smoothing spline  $\kappa$  surface and errors of Fig. 1, and the resampled gas temperature profile. The  $\sigma_r^2(r)$  profiles can now be calculated for each sample, and hence the  $\beta(r)$  profiles.

The results are shown in the bottom panel of Fig. 8 for all eight arms of Perseus, i.e. the full set. The coloured curves represent the  $\beta(r)$  median Monte Carlo profiles obtained from the individual sectors of the Perseus data, and the black dashed curve shows another LOESS smoothing to these curves to infer an overall  $\beta$  for the data included. The inner dark grey band shows the  $1\sigma$  standard error of the mean as obtained via the standard deviation of the LOESS fit, and the light grey outer bands the additional  $1\sigma$  standard error of the mean from the standard deviation of the  $\beta$  obtained from the RAMSES mock data as seen in the left-hand side of Fig. 6. We see that the  $\beta$  profile ranges from 0 in the inner parts towards 1 at  $r_{200}$  where uncertainty grows large on the data and the validity of our assumptions, and thus on  $\beta$ .

For the partial sets, we perform the same analysis but include only the three sectors of the Urban et al. set, and the five sectors selected



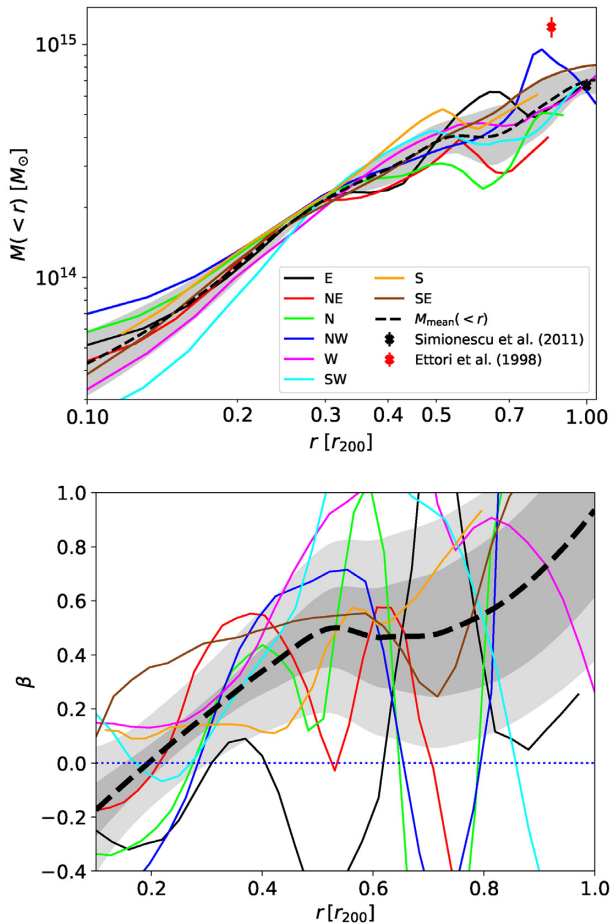


**Figure 8.** Top panel: mass profiles for the eight sectors of Perseus as obtained from hydrostatic equilibrium. The gray band shows the  $1\sigma$  spread of the individual profiles. Note the logarithmic  $r$ -axis. The red point at  $0.85 r_{200}$  shows the Perseus mass estimate from Ettori, Fabian & White (1998), with error bars showing the 10 and 90 per cent from an MC fitting of a  $\beta$  profile to ROSAT data. The black point at  $1.0 r_{200}$  shows the mass estimate and  $1\sigma$  error bars of Simionescu et al. (2011), which is based on NFW-profile fits of the Suzaku data of the north-western and eastern arms only. We note that while our findings do not agree with those of Ettori et al. (1998), they are in agreement with the Simionescu et al. (2011) result. Bottom panel: calculated  $\beta(r)$  profiles for the same directions arms. The dark grey band represents the uncertainty of the mean  $\beta$  profile based on the spread of the Perseus sample ( $\sigma/\sqrt{N}$ , where  $N$  is number of sectors), and the light grey shows the added uncertainty of the mean based on the standard deviation of the RAMSES full set, i.e. the grey area of the left-hand panel of Fig. 6.

through  $T_W$  profiles. The  $\beta$  can be seen in the left- and right-hand panels of Fig. 9, respectively. Here, the grey inner bands represent the same as for the full set, but the outer light grey bands are instead taken from the standard deviation of the right-hand panel of Fig. 6. We see especially for the set chosen here that  $\beta$  is different from 0 between  $0.3 r_{200}$  and  $0.6 r_{200}$  beyond its standard error. Including all the error bars, we have here found indications that the velocity anisotropy in Perseus is of the order

$$\beta_{r=0.5r_{200}} = 0.5 \pm 0.1 \pm 0.2, \quad (13)$$

where the error bars are from variations within the Perseus cluster sectors, and the added scatter from the hydrostatic equilibrium technique itself as applied on each individual arm. This takes the optimistic stand that sectors within a galaxy cluster are completely

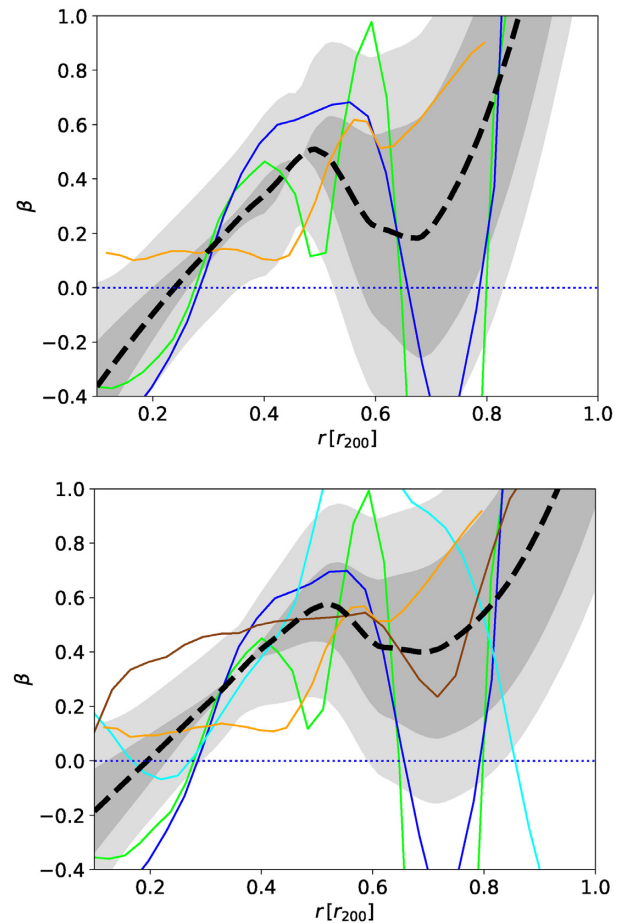


**Figure 9.** Top panel:  $\beta(r)$  using only the selected three sectors that are classified as ‘Relaxed’ in Urban et al. (2014). Bottom panel:  $\beta(r)$  using the five equilibrated sectors according to Section 8. In both figures, the black dashed curve shows LOESS fit to the profiles. The dark grey inner band shows the uncertainty of the mean  $\sigma/\sqrt{N}$ , where  $\sigma$  is the spread as obtained through LOESS generalized cross-validation, and  $N$  is the number of sectors included. The light grey outer band shows the added uncertainty from spread of the RIGHT-HAND SIDE of Fig. 6, i.e. the uncertainty from the inference technique itself. For each sector, multiple  $\beta$  profiles are calculated via the analytical framework and MC bootstrap procedure described in this paper. Slight variations upon each MC realization occurs, and so the profiles may be slightly different between realizations.

uncorrelated inferences of  $\beta$ . Taking the more pessimistic viewpoint that sectors within a single cluster are completely correlated yields  $\beta_{r=0.5r_{200}} = 0.5 \pm 0.1 \pm 0.3$ . This includes uncertainty from temperature measurements and uncertainty in  $\kappa$ . From around  $0.6 r_{200}$  and up to  $0.8 r_{200}$ , the inference of  $\beta$  is consistent with 0, and beyond that the error grows as the assumptions of hydrostatic equilibrium breaks down even for the selected clusters and sectors within them. This in fact is already seen in the mass profiles of the RAMSES clusters, where the hydrostatic method has large error bars at these large radii. Generally  $\beta$  tends to increase with increasing radius. At  $r < 0.2 r_{200}$ , the results are statistically consistent with  $\beta = 0$ , but if the decrease extends to lower radii, it could be interpreted as an effect of the brightest central galaxy making orbits more tangentially biased. However, this effect should not be visible at the scales examined in this work (Host & Hansen 2011). Fig. 10 compares the Perseus inference to the  $\beta$  profile of the chosen sectors of the RAMSES clusters,

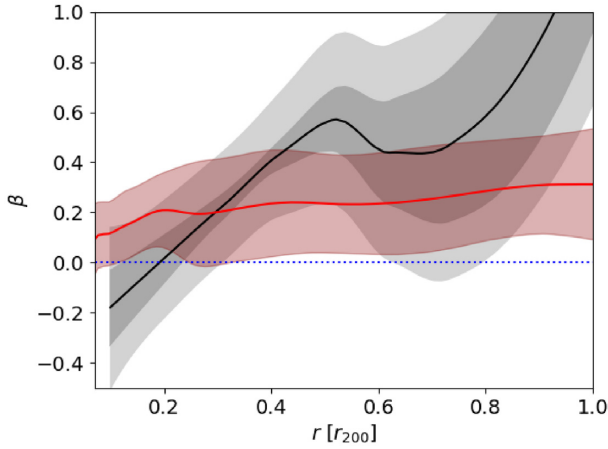


**Figure 10.** Comparison of the true  $\beta$  profile from RAMSES (red curve) and the inferred  $\beta$  profile for Perseus (black curve). The RAMSES profile is comprised of the  $\beta$  profiles of the relaxed sectors of the relaxed clusters as also shown in the right-hand panel of Fig. 6. The Perseus profile is the same as shown in the bottom panel of Fig. 9 for the five arms selected through our analysis. Again, the dark grey inner band shows the uncertainty of the mean  $\sigma/\sqrt{N}$ , where  $\sigma$  is the standard deviation as obtained through LOESS generalized cross-validation, and  $N$  is the number of sectors included. The light grey outer band shows the added uncertainty from spread of the right-hand side of Fig. 6, i.e. the uncertainty from the inference technique itself.

and again we see, for this single Perseus inference, that observation and simulation agrees within  $r_{200}$ .

It is worth keeping in mind that  $\beta$ , in principle, could take on any value between  $+1$  and  $-\infty$ . The simulated values of  $\beta$  from these 51 RAMSES clusters are about 0.25 at  $r = 0.5r_{200}$  (with a  $1\sigma$  spread about 0.2 among the 51 clusters), and at  $r \sim r_{200}$  it is about 0.35 (with a dispersion about  $^{+0.2}_{-0.4}$ ). Upon comparing the inferred  $\beta$  with the  $\beta$  of the simulated clusters in Figs 6 and 9, respectively, we see that they are in reasonable agreement at least until  $0.7r_{200}$ . Another way to visualize the velocity anisotropy parameter is through joining  $\sigma_r^2$  and  $\sigma_t^2$  in the construct

$$\beta_j = \frac{\sigma_r^2 - \sigma_t^2}{\sigma_r^2 + \sigma_t^2} = \frac{\beta}{2 - \beta}, \quad (14)$$

which ranges from  $-1$  to  $1$ . Fig. 11 shows precisely this quantity for the five sectors of the Perseus cluster selected here, where the  $\beta_j$  profile with its standard error of the mean is seen to be non-trivial below  $0.6r_{200}$ .

It should be noted that in spite of removing data from the analysis, the Perseus resulting  $\beta$  is comparable to that of the one with the full data both in terms of the mean curve and the error. Perseus is itself a virialized cluster, and thus expectations of bettering the  $\beta$  inference remarkably with this data selection technique are low. However, as multiple clusters are discovered and analysed through the same technique, our results from the RAMSES simulation show that it is possible to better the uncertainty in  $\beta$  inferences by conducting data selection of the type outlined here. Høst et al. obtained inferences of  $\beta$  within  $r_{2500}$  for a stack of 16 clusters observed in X-ray (Host et al. 2009), whereas here we analyse just one single cluster. In the future, we hope to include future cluster X-ray observations to high radii to further bring uncertainties down.

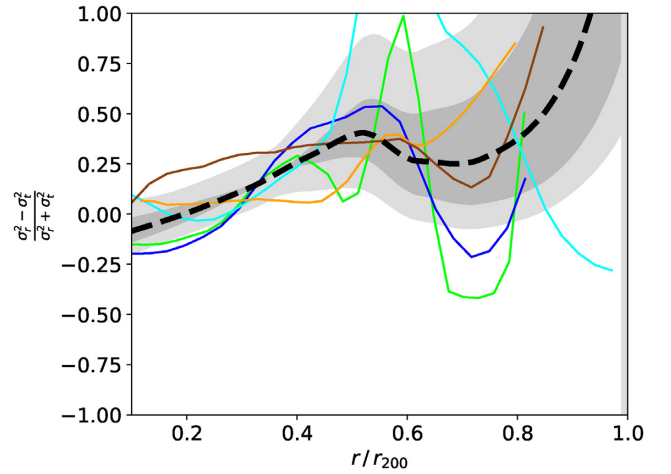


**Figure 11.** The non-standard and symmetrized  $\beta_j$ , which can only assume values between  $-1$  and  $+1$ , plotted for the five sectors of Perseus selected in this work through  $T_W$ . The black dashed line shows the LOESS fit to the five profiles. The inner and outer grey bands show the standard errors of the mean similarly to the ones of Fig. 8.

## 10 CONCLUSION

The DM velocity anisotropy contains information on the dynamics of DM in equilibrated structures. By combining the gas equation from hydrostatic equilibrium and the DM equation, i.e. the Jeans equation with input from a numerical cosmological simulation that includes the baryonic component, we are able to test the consistency of the velocity anisotropy inference for Perseus with the DM model employed in this simulation. We find that the velocity anisotropy of Perseus is consistent with that of the cosmological model employing a  $\Lambda$ CDM cosmology, lending support to the cold and collisionless nature of DM in galaxy clusters. Our analysis of the Perseus data agrees with previous inferences on the velocity anisotropy. Previous studies employ the strength of a catalogue of 16 galaxy clusters. However, since deprojected gas profiles are requirement of the analysis, the results were within  $0.85r_{2500}$ . The quality and radial extent of the Perseus data allows us to probe the consistency of the DM model towards the virial radius. By analysing and including only sectors of the cluster that displays a well-behaved radial X-ray signal, we show that we in simulation are able to put better constraints on the velocity anisotropy inferences; however, for Perseus, we are only able to get meaningful constraints towards  $0.6r_{200}$ , which is still a large improvement of about a factor of 3 compared to previous work.

The method comes with some caveats: A relation  $\kappa$  from numerical simulations between the gas temperature and the DM total velocity dispersion, i.e. the ‘DM temperature’ is used to calibrate the inference of the DM velocity anisotropy. The inferred velocity anisotropy of a galaxy cluster in observation is only ever as good as the  $\kappa$  that it is calibrated against. Since we assume a DM model in all cosmological simulations, we at best are able to infer velocity anisotropy as relying on the assumptions of the simulation. Therefore, our velocity anisotropy inference should be viewed as a check of consistency with the model employed in the estimation of the total DM velocity dispersion. Furthermore, the Perseus data comprise of just a single galaxy cluster. To obtain better constraints on the DM velocity anisotropy is a statistical challenge, and even a couple of galaxy cluster data sets of the same quality would strengthen the analysis greatly.

Our final remarks concern future analyses. Above we have made the assumption of hydrostatic equilibrium. It is well known that departure from hydrostatic equilibrium impacts the mass determinations; see e.g. Nelson, Lau & Nagai (2014) for a list of references, and also that the velocity anisotropy directly or through mass profiles may depend on orientation (Sparre & Hansen 2012; Wojtak, Gottlöber & Klypin 2013; Svensmark, Hansen & Wojtak 2015). We also assume sphericity of the cluster that has previously been found to impact mass estimates of clusters. Perseus was chosen because it does have a relaxed appearance, and we have chosen only the five most relaxed arms. Furthermore, at the moment, the large scatter in  $\kappa$  leads to large error bars of  $\beta$ . By analysing cones in numerical simulated clusters, for instance, separating according to differences in temperature profiles such as cool-core (CC) and non-CC cones, one might be able to reduce scatter in  $\kappa$ , and hence obtain smaller error bars of the DM  $\beta$ .

Few alternative methods to estimate the DM velocity anisotropy exists (Lemze et al. 2012; Mamon, Boué & Biviano 2013). Future analyses that would improve on the method discussed here could be forced to attempt to improve on the mass determination by including complementary observation e.g. from lensing or the SZ effect (Kneib & Natarajan 1996; Stark, Miller & Halenka 2017). Here one will, however, have to deal with the difficult systematic effects when combining such different observational techniques.

## ACKNOWLEDGEMENTS

It is a pleasure thanking Ondrej Urban for providing the data from Perseus. We thank Adam Mantz, Aurora Simionescu, and Ondrej Urban for constructive suggestions. SHH wishes to thank Christoffer Bruun-Schmidt, Beatriz Soret, and Lasse Albæk for discussions. This project is partially funded by the Danish Council for Independent Research under the project ‘Fundamentals of Dark Matter Structures’, DFF - 6108-00470.

## DATA AVAILABILITY

The data underlying this paper are available in this paper.

## REFERENCES

Agnes P. et al., 2015, *Phys. Lett. B*, 743, 456  
 Albæk L., Hansen S. H., Martizzi D., Moore B., Teyssier R., 2017, *MNRAS*, 472, 3486  
 Amorisco N. C., Zavala J., de Boer T. J. L., 2014, *ApJ*, 782, L39  
 Armitage T. J., Kay S. T., Barnes D. J., Bahé Y. M., Dalla Vecchia C., 2018, *MNRAS*, 482, 3308  
 ATLAS Collaboration, Aad G., Abbott B., Abdallah J., Abdel Khalek S., 2015, *Eur. Phys. J. C*, 75, 92  
 Benítez-Llambay A., Frenk C. S., Ludlow A. D., Navarro J. F., 2018, *MNRAS*, 488, 2387  
 Binney J., Tremaine S., 2008, *Galactic Dynamics*, 2nd edn. Princeton Univ. Press, Princeton  
 Bose S. et al., 2018, *MNRAS*, 486, 4790  
 Brinckmann T., Zavala J., Rapetti D., Hansen S. H., Vogelsberger M., 2018, *MNRAS*, 474, 746  
 Bullock J. S., Oñorbe J., Boylan-Kolchin M., Hopkins P. F., Kereš D., Faucher-Giguère C.-A., Quataert E., Murray N., 2015, *MNRAS*, 454, 2092  
 Böhm C., Riazuelo A., Hansen S. H., Schaeffer R., 2002, *Phys. Rev. D*, 66, 083505  
 Clowe D., Bradac M., Gonzalez A. H., Markevitch M., Randall S. W., Jones C., Zaritsky D., 2006, *ApJ*, 648, L109

Di Cintio A., Tremmel M., Governato F., Pontzen A., Zavala J., Bastidas Fry A., Brooks A., Vogelsberger M., 2017, *MNRAS*, 469, 2845  
 Dutton A. A., Macciò A. V., Buck T., Dixon K. L., Blank M., Obreja A., 2018, *MNRAS*, 486, 655  
 Ettori S., Fabian A. C., White D. A., 1998, *MNRAS*, 300, 837  
 Faham C., 2014, preprint ([arXiv:1405.5906](https://arxiv.org/abs/1405.5906))  
 Falco M., Mamon G. A., Wojtak R., Hansen S. H., Gottlöber S., 2013, *MNRAS*, 436, 2639  
 Fitts A. et al., 2018, *MNRAS*, 479, 319  
 Gifford D., Miller C. J., 2013, *ApJ*, 768, L32  
 Gilmore G., Wilkinson M. I., Wyse R. F. G., Kleyna J. T., Koch A., Evans N. W., Grebel E. K., 2007, *ApJ*, 663, 948  
 González-Samaniego A. et al., 2017, *MNRAS*, 472, 2945  
 Hansen S. H., Piffaretti R., 2007, *A&A*, 476, L37  
 Hansen S. H., 2009, *ApJ*, 694, 1250  
 Hansen S. H., Moore B., Zemp M., Stadel J., 2006, *J. Cosmol. Astropart. Phys.*, 2006, 014  
 Hansen S. H., Macciò A. V., Romano-Díaz E., Hoffman Y., Brügggen M., Scannapieco E., Stinson G. S., 2011, *ApJ*, 734, 62  
 Hinshaw G. et al., 2013, *ApJS*, 208, 19  
 Host O., Hansen S. H., 2011, *ApJ*, 736, 52  
 Host O., Hansen S. H., Piffaretti R., Morandi A., Ettori S., Kay S. T., Valdarnini R., 2009, *ApJ*, 690, 358  
 Kay S. T., Da Silva A. C., Aghanim N., Blanchard A., Liddle A. R., Puget J.-L., Sadat R., Thomas P. A., 2007, *MNRAS*, 377, 317  
 Kneib J.-P., Natarajan P., 1996, *MNRAS*, 283, 1031  
 Lemze D. et al., 2012, *ApJ*, 752, 141  
 Liu H., Slatyer T. R., Zavala J., 2016, *Phys. Rev. D*, 94, 063507  
 Lowette S., CMS Collaboration, 2016, *Nuclear and Particle Physics Proceedings*, 273, 503  
 Mamon G. A., Boué G., Biviano A., 2013, *MNRAS*, 429, 3079  
 Markevitch M., Vikhlinin A., 2007, *Phys. Rep.*, 443, 1  
 Martizzi D., Agrusa H., 2016, preprint ([arXiv:1608.04388](https://arxiv.org/abs/1608.04388))  
 Martizzi D., Mohammed I., Teyssier R., Moore B., 2014, *MNRAS*, 440, 2290  
 Navarro J. F. et al., 2010, *MNRAS*, 402, 21  
 Nelson K., Lau E. T., Nagai D., 2014, *ApJ*, 792, 25  
 Planck Collaboration et al., 2018, *A&A*, 641, 67  
 Pointecouteau E., Arnaud M., Pratt G. W., 2005, *A&A*, 435, 1  
 Salucci P., Lapi A., Tonini C., Gentile G., Yegorova I., Klein U., 2007, *MNRAS*, 378, 41  
 Santos-Santos I. M., Di Cintio A., Brook C. B., Macciò A., Dutton A., Domínguez-Tenreiro R., 2017, *MNRAS*, 473, 4392  
 Sarazin C. L., 1986, *Rev. Mod. Phys.*, 58, 1  
 Scrucra L., 2011, *Comput. Stat. Data Anal.*, 5, 3010  
 Simionescu A. et al., 2011, *Science*, 331, 1576  
 Simionescu A. et al., 2012, *ApJ*, 757, 182  
 Sparre M., Hansen S. H., 2012, *J. Cosmol. Astropart. Phys.*, 2012, 042  
 Stark A., Miller C. J., Halenka V., 2017, *ApJ*, 874, 10  
 Svensmark J., Hansen S. H., Wojtak R., 2015, *MNRAS*, 448, 1644  
 Teyssier R., 2002, *A&A*, 385, 337  
 Teyssier R., Pontzen A., Dubois Y., Read J. I., 2013, *MNRAS*, 429, 3068  
 Urban O. et al., 2014, *MNRAS*, 437, 3939  
 Vikhlinin A., Kravtsov A., Forman W., Jones C., Markevitch M., Murray S. S., Speybroeck L. V., 2006, *ApJ*, 640, 691  
 Wang X.-F., 2010, *fANCOVA: Nonparametric Analysis of Covariance*, <https://CRAN.R-project.org/package=fANCOVA>  
 Wetzel A. R., Hopkins P. F., Hoon Kim J., Faucher-Giguère C.-A., Kereš D., Quataert E., 2016, *ApJ*, 827, L23  
 Wheeler C. et al., 2018, *MNRAS*, 490, 4447  
 Wojtak R., Gottlöber S., Klypin A., 2013, *MNRAS*, 434, 1576  
 Zavala J., Vogelsberger M., Walker M. G., 2013, *MNRAS*, 431, L20

This paper has been typeset from a  $\text{\LaTeX}$  file prepared by the author.